Journal of Materials Chemistry A

ROYAL SOCIETY OF CHEMISTRY

PAPER

Published on 08 September 2025
Licence and permissions

Check for updates

Cite this: J. Mater. Chem. A, 2025, 13, 33947

SiOC ceramic aerogels with high optical transparency and ultralow thermal conductivity for solar power application

Adane Muche Abebe, *[a] Mattia Biesuz, [a] Cekdar Vakifahmetoglu,[b] Michele Cassetta,[ac] Alessandro Martucci [d] and Gian Domenico Sorarù[a]

Received 17th July 2025
Accepted 8th September 2025

DOI: 10.1039/d5ta05778g

rsc.li/materials-a

Transparent SiOC aerogels were synthesized from methylene-bridged and Si–H-containing preceramic aerogels after pyrolysis in an Ar–H_2 atmosphere at 800 °C and 1000 °C. The presence of Si–H groups in the starting hybrid aerogel facilitates the incorporation of carbon into the amorphous silicon oxycarbide network, thereby reducing the tendency for free carbon formation and enabling the synthesis of transparent silicon oxycarbide aerogels. Various characterization techniques, including FTIR, Raman spectroscopy and SEM, are applied to analyze the structural and microstructural features of the porous materials. Nitrogen physisorption was employed to characterize the surface area, pore volume, and pore size distributions of the SiOC. All samples exhibit high surface areas, ranging from 915 to 1300 $m^2\ g^{-1}$ at 800 °C and from 565 to 855 $m^2\ g^{-1}$ at 1000 °C. The thermal conductivity ranges from 15 to 60 mW m^{-1}-K for samples pyrolyzed at 800 °C and from 35 to 156 mW m^{-1}-K for those treated at 1000 °C. Furthermore, the normalized transmittance of the SiOC aerogels is approximately 91 ± 2% at 780 nm and 95 ± 1% at 900 nm, respectively, for an equivalent thickness of 1 mm. The combination of low thermal conductivity, high transmittance in the visible-NIR range, strong infrared absorption, and excellent microstructural stability at high temperatures makes SiOC aerogels exceptional candidates for solar power tower applications.

Introduction

Polymer-derived ceramics (PDCs) are innovative materials primarily fabricated from silicon-based preceramic polymers. The molecular structure of these preceramic polymers significantly influences the macroscopic chemical and physical properties of the resulting PDCs.[1] Among the various types of PDCs, silicon oxycarbide (SiOC) and silicon carbonitride (SiCN) ceramics exhibit unique properties rarely attainable in other materials.[2] SiOC and SiCN ceramics contain excess free carbon, which depends on the amount of carbon present in the initial precursor and on the pyrolysis parameters.[1–3]

Silicon oxycarbide (SiOC) glass, an anionic modification of silica produced *via* the pyrolysis of hybrid silica gels,[4] demonstrated increased viscosity and a higher glass transition temperature than pure SiO_2. Numerous studies have demonstrated the feasibility of processing SiOC aerogels, which remain stable at high temperatures and offer a promising solution to sintering issues observed in silica aerogels at elevated temperatures.[5] The fabrication of SiOC aerogels typically involves the following steps: (1) synthesis of the wet gel either *via* the sol–gel process[6] or pre-ceramic Si-containing polymer,[7,8] (2) supercritical CO_2 drying and (3) polymer-to-ceramic transformation through pyrolysis in an inert atmosphere at high temperatures ($T \geq 800$ °C).[7]

This study synthesized sol–gel-derived hybrid silica aerogels from a mixture of CH_2-bridged and Si–H containing silicon alkoxides. Compared to the more common methyl-modified silicon alkoxide, the bridged alkoxide provides a lower amount of bonded carbon. At the same time, the Si–H precursor facilitates the incorporation of carbon into the inorganic SiOC network during pyrolysis.[9] Accordingly, both features, *i.e.*, low starting C and use of Si–H moieties, enable the synthesis of SiOC materials with minimal free carbon,[10,11] potentially leading to transparent aerogel. In particular, when the number of C–H bonds equals the number of Si–H bonds in the starting preceramic polymer, the resulting SiOC glass should be a stoichiometric silicon oxycarbide glass, free of any excess carbon phase.[12]

Various forms of transparent aerogels provide excellent thermal insulation and optical clarity, making them promising

[a]Department of Industrial Engineering, University of Trento, Via Sommarive 9, 38123, Trento, Italy. E-mail: adanemuche.abebe@unitn.it
[b]Faculty III Process Sciences, Institute of Material Science and Technology, Chair of Advanced Ceramic Materials, Technische Universität Berlin, 10623, Berlin, Germany
[c]Department of Engineering for Innovation Medicine, University of Verona, 37134 Verona, Italy
[d]Department of Industrial Engineering, University of Padova, Via Marzolo 9, 35131 Padova, Italy

materials for superior thermal insulation in construction applications.[13,14] Recently, multiple studies have been undertaken to employ these materials in non-concentrating solar thermal technologies.[15–18] Inserting transparent aerogels between a glass and an absorber facilitates the transmission of sunlight through the nanostructure, enabling direct conversion into heat. In contrast to concentrating solar power, the receiver in non-concentrating solar power does not require a specialized surface or vacuum enclosure. In non-concentrated solar systems, the radiation emitted from the receiver is absorbed and scattered throughout the aerogel network, rather than only at the surface, and is subsequently re-emitted back to the receiver. Consequently, the aerogels function as volumetric radiation shielding, which reduces radiative heat losses and enhances the thermal insulation performance of the thermal receiver, attaining temperatures of up to 350 °C under unconcentrated solar flux.

Transparent, thermally insulating aerogels have several promising applications in solar power systems. They can serve as thermal insulation layers in solar thermal collectors[15,19] and photovoltaic/thermal (PV/T) collectors,[18] where they reduce heat loss while maintaining high light transmission. They are also suitable for windows in building-integrated solar thermal systems,[20] where both light transmission and thermal insulation are critical. Furthermore, their volumetric radiation shielding capability enables more efficient operation of high-temperature receivers in concentrated solar power systems, including next-generation supercritical CO_2 receivers.[21]

In our previous studies, transparent SiOC aerogel was obtained when a fragment of the hybrid gel from bis(triethoxysilyl) methane was pyrolyzed in H_2 atmosphere.[10,12] In the present study, we aimed to synthesize transparent monolithic SiOC aerogels treated in an Ar–H_2 atmosphere at 800 °C (see Fig. 1b), targeting ultralow thermal conductivity. The transparency and ultralow thermal conductivities of the SiOC aerogels were achieved through meticulous adjustments to the initial composition of the starting aerogels. We characterized the structural, microstructural, optical, and thermal properties of transparent SiOC aerogels. Thermal diffusivity and conductivity are measured as a function of temperature, up to 500 °C, while optical transmittance is evaluated in the 190–2500 nm range. The results reveal a favorable combination of low thermal conductivity, high transmittance in the visible-to-near-infrared (Vis–NIR) range, and strong absorption beyond 3 μm. These properties, along with excellent thermal stability, make SiOC aerogels promising candidates for solar power applications.

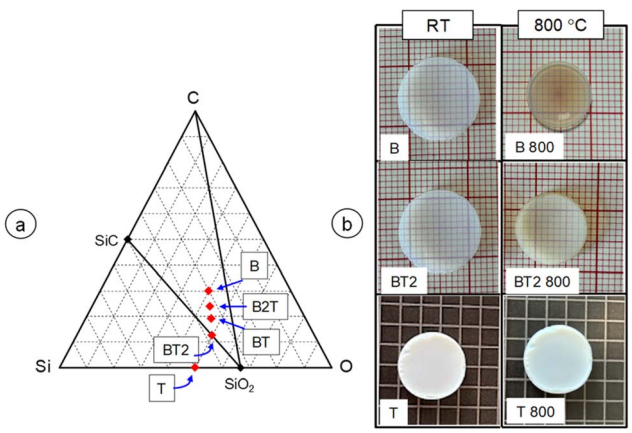

Fig. 1 (a) Theoretical atomic composition of preceramic aerogels represented in the Si–O–C ternary phase diagram. (b) Micrograph of selected hybrid aerogels and SiOC ceramics aerogels treated at 800 °C.

Experimental

SiOC aerogel synthesis

Five silica-based hybrid aerogels with BTEM/TREOS molar ratios of 1/0 (pure BTEM), 2/1, 1/1, 1/2, and 0/1 (pure TREOS) were prepared and labeled B, B2T, BT, BT2, and T, respectively. A detailed description of preceramic aerogel synthesis can be found in our previous work.[22] The corresponding porous ceramics were designated as B x, B2T x, BT x, BT2 x, and T x, respectively, where x represents the pyrolysis temperature (x = 800 or 1000 °C). Notably, the carbon content in the synthesized aerogels decreases with increasing amounts of TREOS see Fig. 1a. The BT2 aerogel, with a (Si–H)/(C–H) molar ratio of 1, is expected to yield stoichiometric SiOC after pyrolysis[12] *i.e.* without the presence of a free carbon phase, whereas the aerogel derived from pure TREOS, which lacks any Si–C bonds, is anticipated to produce understoichiometric silica (Si/SiO_2)[23] (refer to Fig. 1a). Furthermore, aerogels with BTEM/TREOS = 2 and 1 (molar ratio) should lead to a SiOC glass with a small amount of free carbon content of ~3 and 2 wt% after pyrolysis, respectively.

Pyrolysis was conducted in an alumina Lindberg/Blue tube furnace under an Ar-5% H_2 flow at 200 cm^3 min^{-1}, with a heating rate of 1 °C min^{-1}, reaching 800 or 1000 °C. Following a 1 h soaking period at maximum temperature, the samples were cooled to room temperature at 2 °C min^{-1}.

Characterization

The bulk density (ρ_b) and skeleton density (ρ_s) of the pyrolyzed samples were determined using Archimedes' principle with ethanol as the buoyancy solvent, utilizing an analytical balance (Gibertini) with a sensitivity of 0.1 mg. The porosities (ϕ) of samples were computed from the density measurements using the equation: $(1 - (\rho_b/\rho_s)) \times 100\%$.

Fourier transform infrared (FT-IR) spectra were obtained using a Thermo Optics Avatar 330 instrument (Thermo Fischer Scientific, Waltham, MA, USA) on KBr pellets. The spectra were measured in the range of 4000–400 cm^{-1} based on transmittance, with 64 scans and a resolution of 4 cm^{-1}.

Gas adsorption–desorption isotherms for the pyrolyzed samples were conducted using a Quantachrome Instrument (Anton Paar, USA) with nitrogen utilized as the adsorbate gas at 77 K. About 25 mg of samples were employed for physisorption measurements. All the samples were degassed at 350 °C for 7 h to eliminate moisture adsorbed on the surface of the pores. The final mass after degassing was employed for all the calculations.

The surface area was calculated using the micropore BET assistant to select points within the linear range of the BET equation. The cumulative pore volume and pore diameter range were obtained using the density functional theory (DFT).

The weight change during the polymer-to-ceramic transformation was examined through thermogravimetric analysis (TGA) on a Netzsch STA 409 instrument (Netzsch-Geratebau GmbH, Selb, Germany). The mass variation was recorded as a function of temperature up to 1000 °C with a flow of Ar-5% H_2 gas at 100 cm^3 min^{-1}, and a heating rate of 10 °C min^{-1}.

The microstructure of SiOC aerogels was characterized using an FE-SEM Supra 40 Zeiss (Carl Zeiss, Oberkochen, Germany) on fresh fracture surface was coated with a thin Pt/Pd (80 : 20) film.

X-ray diffraction (XRD) spectra were collected on powder samples utilizing an IPD3000 diffractometer equipped with a Cu anode source operating at 40 kV and 30 mA coupled to a multilayer monochromator (Goebel mirror). The spectra were acquired over the $2\theta = 10$–80° range, with a 0.02° step size and 1200 s acquisition time, using a Dectris Mythen 1K hybrid pixel detector.

Raman spectra were acquired employing a Thermo Scientific DXR2 (Madison, WI, USA) equipped with a diode-pumped solid-state (DPSS) laser ($\lambda = 532$ nm). The spectra were recorded over the 100–3500 cm^{-1} range with a resolution of 4 cm^{-1}. The laser power was set at its minimum value and increased stepwise to avoid thermal degradation induced by the laser power. Subsequently, measurements were conducted at 10 mW with 30 accumulations of 20 seconds each.

The thermal diffusivity (α) of SiOC samples was determined using the Laser Flash Analysis, LFA, (LFA 467 HT HyperFlash, Selb, Germany). An exponential pulse was applied to the front surface, and temperature changes on the opposite surface were recorded. Thermal diffusivity measurements were conducted on a 10 × 10 × 2.0 mm^3 sample from 20 to 500 °C, utilizing a pulse width of 600 µs and an applied voltage of 250 volts. The thermal diffusivity was calculated based on a linear penetration model. The specific heat capacity (c_p) of SiOC ceramics was assessed using a differential scanning calorimeter (DSC), measured up to 300 °C, with values above this temperature obtained by extrapolation. Due to the porous microstructure of the SiOC aerogels, the samples adsorbed 2 to 5 wt% moisture. Therefore, to eliminate the humidity before the C_p measurement, the samples were heated to 300 °C. Subsequent measurements were carried out up to 300 °C. Finally, the thermal conductivity (λ) was calculated from the thermal diffusivity and heat capacity measurements according to the relation: $\lambda = \rho c_p \alpha$ where ρ is the density, c_p the heat capacity and α the thermal diffusivity.

The optical transmittance of SiOC ceramic was evaluated using a UV-Vis-NIR spectrophotometer (Jasco V770) in the range of 190 to 2500 nm at 400 nm min^{-1}. FTIR spectroscopy measurements were conducted with a Jasco FT-IR 4200 spectrometer. Measurements were collected in transmission mode in the 4500–400 cm^{-1} range, employing 64 scans per min^{-1} and with a resolution of 2 cm^{-1}.

Results and discussion

Thermogravimetric analysis

The preceramic-to-ceramic transformation was followed by thermogravimetric measurements (Fig. 2). TGA curves show that the transformation occurs in three distinct temperature regimes. Weight loss observed up to 200 °C is attributed to the release of water and ethanol from residual terminal Si–OH and Si–OEt groups, as well as from residual solvent. The intensity of this initial weight loss step decreases with increasing *T* content, suggesting that compositions with a higher amount of T precursor contain fewer unreacted terminal Si–OH/Si–OEt groups. This indicates the formation of a more condensed siloxane network. Indeed, T aerogel indicates no weight loss up to 300 °C, supporting the hypothesis that it is fully crosslinked.

Between 400 °C and 600 °C, a significant mass loss occurs, primarily attributed to the release of Si-containing molecules, such as silanes, which are generated by redistribution reactions involving Si–O, Si–C, and Si–H bonds.[24–26] A third weight loss is observed between 700 and 900 °C, resulting from the mineralization reactions that release CH_4 and H_2 (ref. 25) gases. Overall, the mass lost across these three temperature ranges tends to increase with the amount of BTEM present in the starting aerogel.

Microstructural characterization

Density

Table 1 shows the bulk density, skeletal density and porosity of the SiOC aerogels pyrolyzed in Ar–H_2 flow at 800 and 1000 °C. The skeletal densities of the SiOC aerogels increase with pyrolysis temperature but remain similar regardless of the chemical composition. Whereas, the bulk density of SiOC

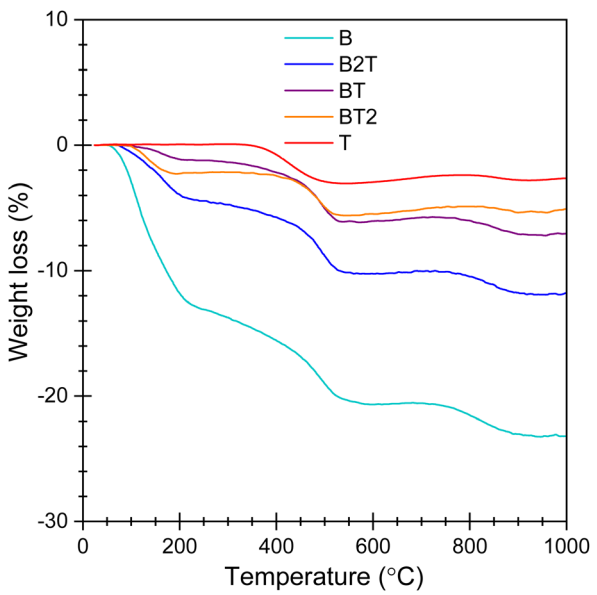

Fig. 2 TGA curve of the hybrid silica aerogels in Ar–H_2 atmosphere up to 1000 °C. Aerogels denoted as B, B2T, BT, BT2 and T with BTEM/TREOS molar ratios of 1/0 (pure BTEM), 2/1, 1/1, 1/2, and 0/1 (pure TREOS), respectively.

Table 1 Bulk density (ρ_b), skeletal density (ρ_s), and porosity (ϕ) of SiOC aerogels

Sample	ρ_b [g cm^{-3}] ± 0.02	ρ_s [g cm^{-3}] ± 0.01	ϕ [vol%]
B 800	0.62	2.22	72.0
B 1000	0.89	2.35	62.1
B2T 800	0.40	2.10	81.0
B2T 1000	0.68	2.31	70.5
BT 800	0.38	2.10	82.9
BT 1000	0.52	2.32	75.4
BT2 800	0.25	2.12	88.2
BT2 1000	0.40	2.34	80.9
T 800	0.17	1.82	90.6
T 1000	0.23	2.30	90.0

aerogels depends on both the pyrolysis temperature and initial composition, as shown in Fig. S1a. Increasing the pyrolysis temperature from 800 °C to 1000 °C causes further densification of the SiOC aerogel due to the completion of the mineralization reactions.

N_2 physisorption

The microstructure of porous SiOC aerogels was studied through N_2 physisorption. The adsorption–desorption isotherms of aerogels treated at 800 °C and 1000 °C in an Ar–H_2 atmosphere are depicted in Fig. 3. All the SiOC aerogels exhibit type VI(a) isotherms, characterized by a hysteresis loop attributed to capillary condensation within the mesopore range. The SiOC aerogels treated at both temperatures exhibit a notable increase in adsorbed volume at a lower relative pressure (p/p_0 < 0.05), indicative of microporosity (pore width <2 nm) within their structure. In fact, the volume percentage of micropores ranges from 5 to 17% at 800 °C and 1 to 9% at 1000 °C, as detailed in Table 2. It is worth noticing that, apart from sample T, all other SiOC aerogels did not display macropores (pore width >50 nm).

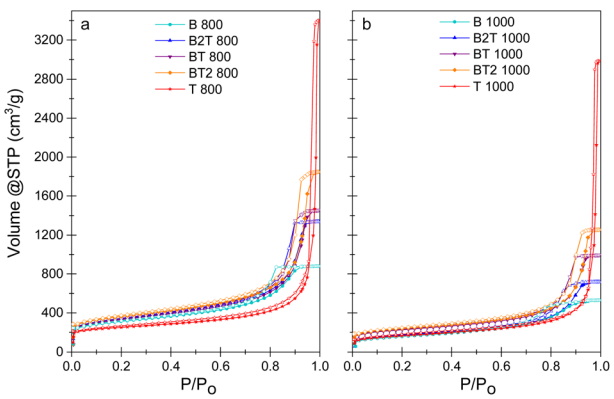

Fig. 3 Nitrogen adsorption–desorption isotherms of SiOC aerogels at (a) 800 °C and (b) 1000 °C.

The BET (Brunauer, Emmett and Teller) specific surface area (SSA), pore width, micro-, meso- and macro-pore volumes of the pyrolyzed aerogels are provided in Table 2 and Fig. S1(b). At 800 °C, the specific surface area (SSA) ranges from approximately 900 to 1300 m^2 g^{-1}, while at 1000 °C it ranges between 565 and 855 m^2 g^{-1}. These exceptionally high values for samples treated at such elevated temperatures further confirm the well-known high-temperature stability of the silicon oxycarbide microstructure.[27] Compared to silica, silicon oxycarbides exhibit a significantly higher viscosity – by 2 to 3 orders of magnitude[28] – which inhibits the densification of the porous aerogel. In contrast, densification of SiO_2 aerogels typically begins at temperatures ≥600 °C.[17]

Fig. 4 shows the DFT pore size distribution of SiOC aerogels treated at pyrolysis temperatures of 800 and 1000 °C. The average pore width of the studied samples is closely correlated to their initial compositions and the pyrolysis temperatures. Notably, samples with higher amounts of TREOS consistently show larger pore diameters. In contrast, as the pyrolysis temperature increases from 800 to 1000 °C, the most probable pore sizes tend to shift slightly to the lower values. At 800 °C, the most probable pore diameters are approximately 12 nm, 16 nm, 20 nm, and 25 nm for B 800, B2T 800, BT 800 and BT2 800, respectively. Except for aerogel T, which has 68% macroporosity, all other samples fall within the mesoporous range (2–50 nm). Similarly, at 1000 °C, the most probable pores and upper limits of pore diameters for the ceramic aerogel shifted to lower values. As depicted in Fig. S2, the average pore diameter exhibits a continuous decline with rising pyrolysis temperatures.

Table 2 Specific surface area (SSA), micropore volume (V_{micro}), mesopore volume (V_{meso}), macropore volume (V_{macro}) and total pore volume (V_{total}) of aerogels pyrolyzed at 800 and 1000 °C in Ar–H_2[a]

Sample	SSA [m^2 g^{-1}]	V_{micro} [cm^3 g^{-1}]	V_{meso} [cm^3 g^{-1}]	V_{macro} [cm^3 g^{-1}]	V_{total} [cm^3 g^{-1}]
B 800	1120	0.23	1.10	0.00	1.33
B 1000	565	0.05	0.75	0.00	0.80
B2T 800	1205	0.18	1.85	0.00	2.03
B2T 1000	635	0.03	1.06	0.00	1.09
BT 800	1180	0.18	2.03	0.01	2.22
BT 1000	810	0.13	1.38	0.00	1.51
BT2 800	1300	0.21	2.58	0.01	2.80
BT2 1000	855	0.14	1.78	0.00	1.92
T 800	915	0.16	1.69	1.15	3.00
T 1000	595	0.04	1.63	1.17	3.38

[a] Please note that the total pore volume of T aerogel at 800 and 1000 °C was determined from the bulk and skeletal density measurements and found to be 5.33 and 3.91 cm^3 g^{-1}, respectively.

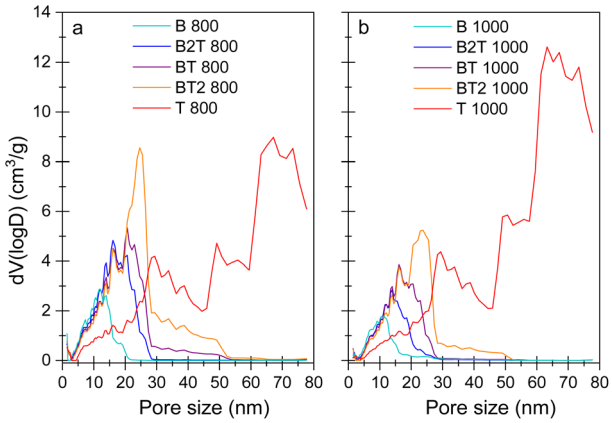

Fig. 4 DFT pore size distributions of the SiOC aerogels pyrolyzed at (a) 800 °C and (b) 1000 °C. Where *V* is the cumulative pore volume and *D* is the pore diameter. At 800 °C, the T 800 glass exhibited 32% mesopores and 69% macropores, while at 1000 °C, the T 1000 sample displayed 42% mesopores and 58% macropores. In both heat treatments, the T glasses demonstrated a large portion of macroporosity in the silica matrix.

The overall pore volume of the SiOC samples is affected by both their compositions and the pyrolysis temperatures. Typically, a higher concentration of TREOS in the starting composition results in a larger pore volume, as shown in Fig. 5. However, as the pyrolysis temperatures rise, the pore volume tends to decrease due to densification (refer to Table S1).

SEM

Fig. 6 presents the SEM micrographs of the aerogels pyrolyzed at 800 and 1000 °C. The SEM shows, for all compositions and temperatures, the typical aerogel microstructure with submicrometric colloidal particles. On the other hand, the compositions rich in B exhibit a more compact microstructure, with no macropores than those clearly visible in the T 800 and T 1000 samples. The TREOS modified samples, specifically BT2 and T aerogels exhibit more open networks, with T showing the highest porosity among all at the respective pyrolysis temperatures. In fact, the microstructure of the ceramic materials is more influenced by the initial compositions than by the pyrolysis temperatures. The results of the SEM observation align well with the bulk densities and the nitrogen physisorption analysis. In particular, the bulk density decreases while the porosity and pore size increase with increasing T content in the samples.

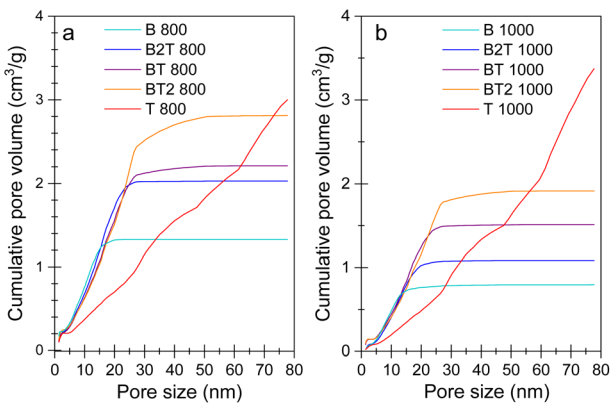

Fig. 5 DFT cumulative pore volume of SiOC aerogels pyrolyzed at (a) 800 °C and (b) 1000 °C. The cumulative pore volume of the SiOC aerogels, as a function of pore diameter, reached saturation for all samples, except for those derived from pure TREOS (T 800 and T 1000 samples), which continued to show an increase. This observation suggests the presence of larger macropores in these samples.

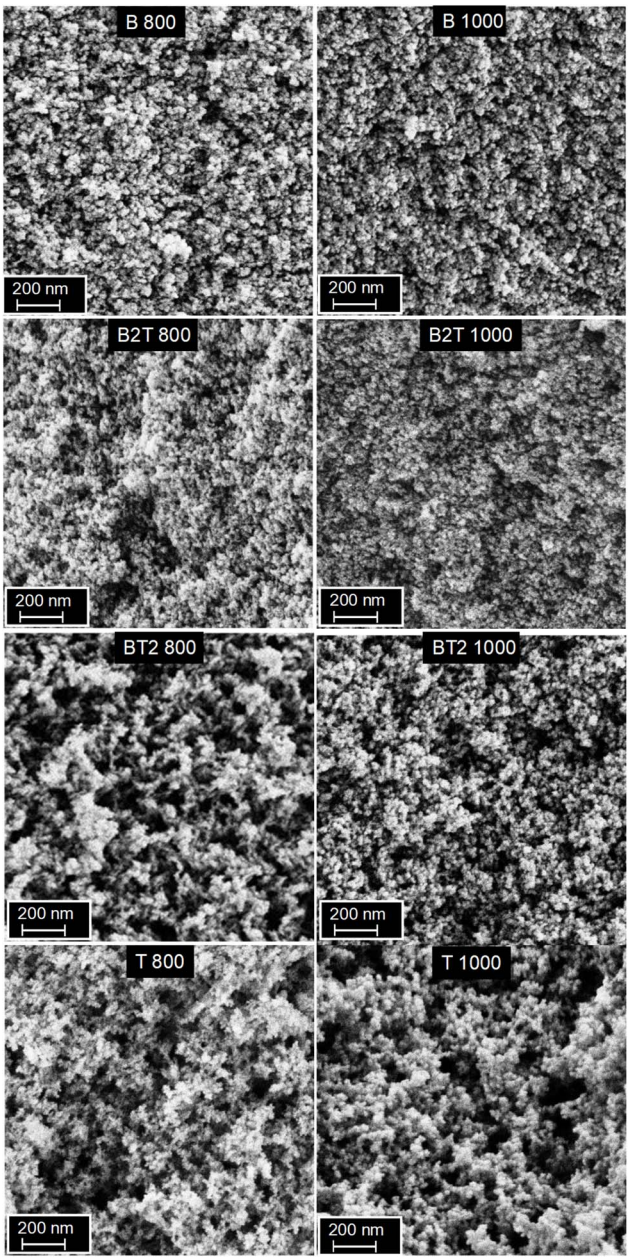

Fig. 6 Field emission scanning electron microscope (FE-SEM) images of the SiOC and Si/SiO2 aerogels pyrolyzed at 800 °C and 1000 °C.

Structural characterization

FT-IR. The infrared spectra of pyrolyzed SiOC aerogels are presented in Fig. 7. At 800 °C, the most intense bands are

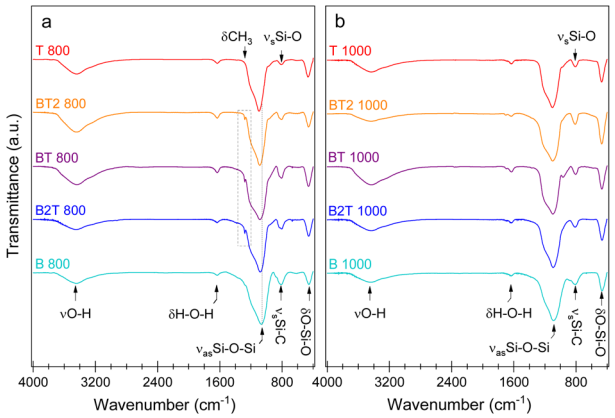

Fig. 7 Infrared spectra of SiOC aerogels treated at (a) 800 °C, and (b) 1000 °C in KBr pellet. The peak at ~810 cm^{-1} in both T 800 and T 1000 samples corresponds to the Si–O bond. The BT 1000 sample exhibits a small peak at 970 cm^{-1} associated with the Si–OH unit.

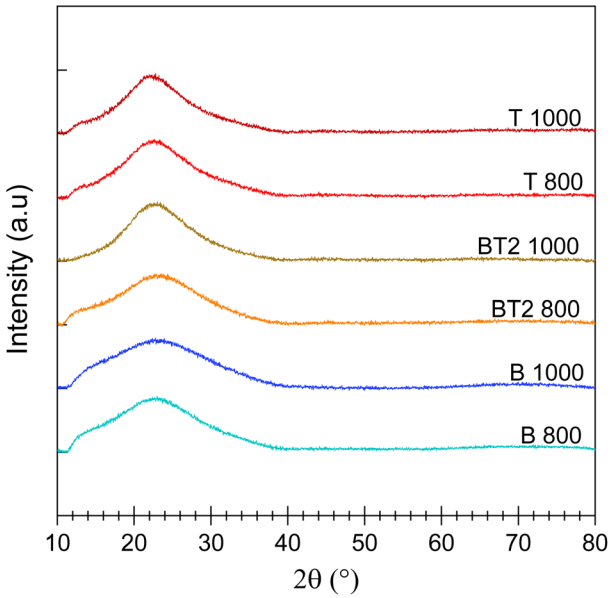

Fig. 8 XRD spectra of B, BT2 and T aerogels pyrolyzed at 800 °C and 1000 °C.

observed in the following ranges: 1065–1095 cm^{-1} (asymmetric stretching, ν_{as}, of Si–O–Si), 805–812 cm^{-1} (stretching, ν, of Si–C and Si–O), and 455–470 cm^{-1} (bending, δ, of O–Si–O). Interestingly, the absorption bands associated with the Si–O bond shift from 1095 cm^{-1} for T-800 (no carbon in the network) to 1065 cm^{-1} for B-800 (exhibiting maximum carbon content). This shift to a lower wavenumber correlates with the insertion of carbon into the silicon oxycarbide network, in agreement with the existing literature.[29] At 800 °C, a new peak at 1279 cm^{-1} appears in $-CH_2-$ and Si–H -containing aerogels, typically attributed to the symmetric bending of CH_3 in the Si–CH_3 units (see Fig. 7a). It is worth noting that Si–CH_3 moieties do not exist in the starting precursors, implying that they form *in situ* during pyrolysis. Similar results have already been reported in the literature.[30]

The infrared spectra of aerogels treated at 1000 °C are depicted in Fig. 7b. Characteristic peaks ranging from 1090 to 1105 cm^{-1} are attributed to the asymmetric stretching vibration of Si–O–Si bonds. Upon pyrolysis at elevated temperatures, the peak position ν_{as}Si–O–Si shifts to higher wavenumbers. The change of the wavenumber position varies among aerogels, typically ranging from 25 to 10 cm^{-1}. It has been reported that the shifting of the peak position to a higher wavenumber is due to an increasing degree of cross-linking during organic-to-inorganic transformations.[31]

Peaks observed at 3450 and 1635 cm^{-1} originate from the O–H group and adsorbed water, respectively. The extremely high surface area of SiOC aerogels, which ranges from 915–1300 $m^2\ g^{-1}$ at 800 °C and 565–855 $m^2\ g^{-1}$ at 1000C, favours moisture adsorption. Additionally, bands associated with Si–CH_3 groups, present at 800 °C, are no longer observed after pyrolysis at 1000 °C, indicating their removal at higher temperatures.

XRD

Fig. 8 shows the XRD spectra of some selected SiOC aerogels treated at 800 and 1000 °C. The spectra up to 1000 °C display a completely amorphous structure, with only a short-ranged order represented by a broad peak at *ca* $2\theta = 22°$, characteristics of amorphous silicates. It was evident that no crystalline phases of carbon, silica, SiC or Si formed within the applied temperature range.

Raman spectroscopy

Fig. 9 presents the Raman spectra of B 800, BT 800 and BT2 800 SiOC aerogels that were treated at 800 °C, while the other

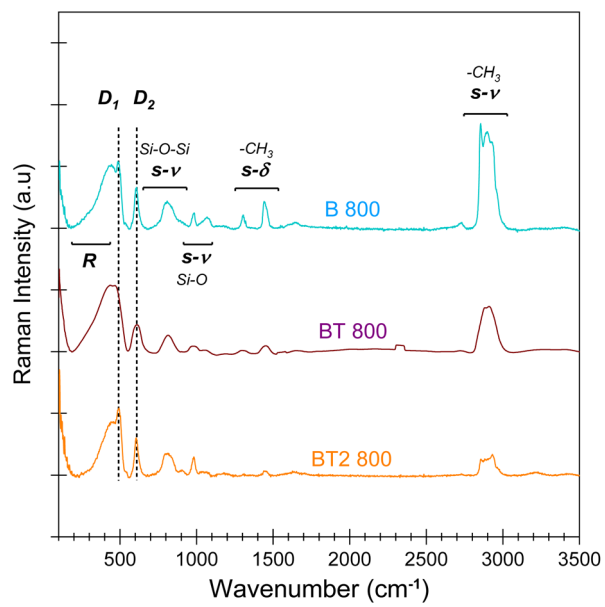

Fig. 9 Raman spectra of B-, BT-, and BT2-800 samples. The D1 and D2 bands correspond to 4-, and 3-membered silicate rings, respectively, while the R band represents a well-resolved Raman band. $S-\nu$ denotes symmetric stretching vibration, and $s-\delta$ indicates symmetric rocking modes.

samples, which were influenced by a strong fluorescent background were not analyzed. Specifically, the following key details were revealed from the measurements:

(1) Aerogels pyrolyzed at 800 °C retained some organic groups within the structure. The Raman peaks at 1300 and 1440 cm^{-1} are associated with symmetric rocking of methyl groups, while bands at 2860 and 2900 cm^{-1} are owing to the symmetric stretching of $–CH_3$ units. The B 800 aerogel shows a higher relative intensity of methyl units compared to the BT 800 and BT2 800 samples.

(2) The SiOC networks exhibit two prominent defect bands, D1 and D2. The D2 band that appeared at 607 cm^{-1} is associated with an $(OSi)_3$-ring breathing mode, while the D1 peak at 490 cm^{-1} belongs to the four-member silicate rings.[32,33] In addition, the SiOC networks display a well-resolved R band, which shows the presence of higher-membered rings of SiO_4 tetrahedral (5 and 5+ membered rings) in the silicon oxycarbide structure. The relative ratio between R and D_1 (higher in B 800) suggests a higher number of 5+ membered rings in the B 800 sample than in BT2 800. In general, the D2 band is extremely sharp and intense compared to the conventional melt-quench-derived silica. Therefore, the SiOC network at 800 °C displays a higher concentration of small-membered rings than silica glass.

(3) The sharp band at about 970 cm^{-1} can be attributed to depolymerized tetrahedral stretching due to the effect of structural water[34] creating Q^3 units in which silicon is bonded to an OH and 3 bridging oxygens.

Thermal and optical properties

Thermal conductivity. The thermal diffusivity of the SiOC aerogels is shown in Fig. 10 as a function of measured temperatures. The thermal diffusivity of the SiOC materials pyrolyzed at 800 °C ranges from 1.0×10^{-3} cm^2 s^{-1} to 2.3×10^{-3} cm^2 s^{-1} measured at 50 °C. The B 800 sample, featuring a higher bulk density, exhibited relatively higher thermal diffusivity values than the others. The thermal diffusivity of SiOC aerogels increased with the pyrolysis temperatures. Both pyrolysis temperatures resulted in a modest increase in thermal diffusivity up to 150 °C, likely due to the evolution of moisture from the porous structure. Beyond 150 °C, as the temperature rises, increased phonon vibration leads to phonon–phonon scattering, which reduces the mean free path and subsequently decreases the thermal diffusivity.[35,36]

The thermal conductivity of porous SiOC aerogels at various temperatures was calculated from the thermal diffusivity, the bulk density and the heat capacity measurements according to the relation.

$$\lambda(T) = \rho(T)C_p(T)\alpha(T)$$

where $\lambda(T)$ – thermal conductivity, $\rho(T)$ – bulk density, $C_p(T)$ – heat capacity and $\alpha(T)$ – thermal diffusivity of porous SiOC samples as a function of temperature.

The density variation as a function of temperature can be ignored due to the low thermal expansion coefficient of silicon oxycarbide (approximately 3.2×10^{-6} $°C^{-1}$).[27] Therefore, the density at room temperature was utilized in the thermal conductivity calculations. Whereas, the specific heat capacity and diffusivity values were obtained from the DSC and LFA measurements, respectively.

The evolution of specific heat capacity for SiOC aerogels as a function of temperature is shown in Fig. 11. The values were measured up to 300 °C and extrapolated from 350 to 500 °C. The measured heat capacity resembles that of the C_p of dense SiOC ceramics[27] (refer to Fig. S3). The extrapolation values for aerogel pyrolyzed at 800 °C are slightly overestimated compared to literature values. The C_p values of SiOC aerogels at 1000 °C are closely associated with the bulk density of the samples. The thermal conductivity of porous SiOC aerogels at 50 °C varies between 15 to 60 mW m^{-1}-K for aerogels pyrolyzed at 800 °C and 35 to 156 mW m^{-1}-K for those pyrolyzed at 1000 °C. In both pyrolysis conditions, the thermal conductivity follows the trend of B > B2T > BT > BT2 across all measured temperatures. The thermal conductivity of aerogels pyrolyzed at 800 °C, appears to be temperature-independent, with approximate values of 80, 30, 25, and 15 mW m^{-1}-K for B 800, B2T 800, BT 800, and BT2 800, respectively (refer to Fig. 12a). The thermal conductivity profiles

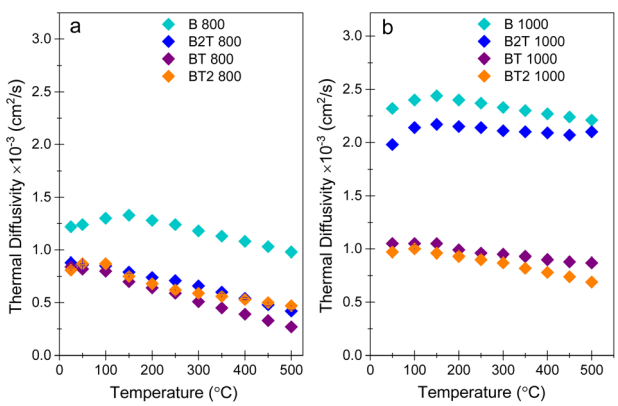

Fig. 10 Thermal diffusivity of the SiOC aerogels pyrolyzed in $Ar–H_2$ atmosphere at (a) 800 °C and (b) 1000 °C. Note that thermal diffusivity could not be measured for the T 800 and T 1000 samples.

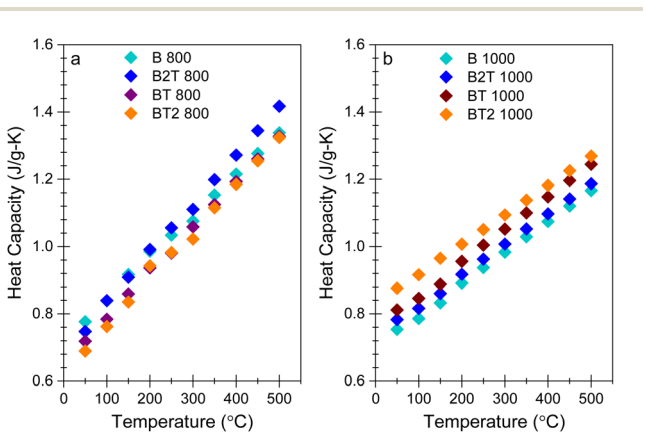

Fig. 11 Specific heat capacity of the SiOC aerogels pyrolyzed at (a) 800 and (b) 1000 °C.

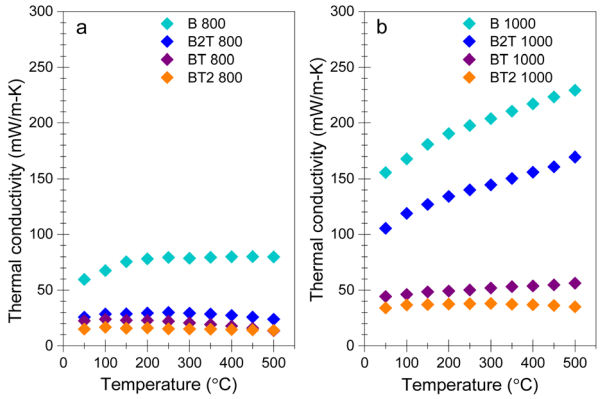

Fig. 12 Thermal conductivity of SiOC aerogels pyrolyzed in Ar–H_2 atmosphere at (a) 800 °C and (b) 1000 °C. The SiOC aerogels (B2T-, BT-, and BT2-800) treated at 800 °C are transparent and their corresponding thermal conductivity remains constant across the temperatures.

for aerogels pyrolyzed at 1000 °C are presented in Fig. 12b. Interestingly, the BT 1000 and BT2 1000 samples exhibit a constant thermal conductivity of approximately 35 mW m^{-1}-K and 50 mW m^{-1}-K, respectively. In contrast, the B 1000 and B2T 1000 aerogels demonstrate: (i) thermal conductivity increases with temperature and (ii) a higher thermal conductivity, which can be attributed to the significant densification and high thermal diffusivity values.

Fig. 13 presents the average thermal conductivity of SiOC aerogels as a function of bulk density. For the sample treated at 800 °C (Fig. 13a), thermal conductivity above 0.35 g cm^{-3} exhibits a strong dependence on the bulk density. Below this threshold, the thermal conductivity was less sensitive to changes in bulk density, as the gas phase dominates heat transfer. This behavior is attributed to the high porosity and limited solid connectivity of the BT2 800 aerogel, as seen in the SEM images in Fig. 6. With increasing pyrolysis temperature to 1000 °C (Fig. 13b), the SiOC aerogels undergo significant structural densification and phase evolution, leading to the formation of a more continuous solid network. Consequently, solid-phase conduction becomes the dominant heat transfer

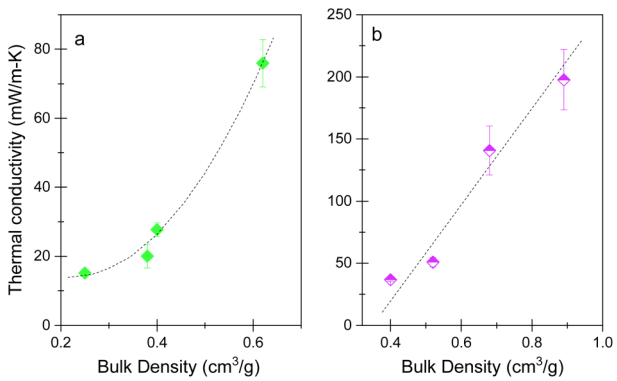

Fig. 13 Average thermal conductivity (50–500 °C) of SiOC aerogels pyrolyzed at (a) 800 °C and (b) 1000 °C as a function of bulk density. The dashed lines are guides for the eye.

mechanism, resulting in a direct proportionality between thermal conductivity and bulk density.

It is important to highlight that BT2 800 exhibits an exceptionally low thermal conductivity of 15 mW m^{-1}-K at 500 °C, which is the lowest value ever reported for ceramic aerogel materials. This value is significantly lower than those of similar systems, such as SiOC foam-aerogel composite (50 mW m^{-1}-k at 500 °C),[37] SiOC aerogel (44 mW m^{-1}-k at 500 °C),[38] and alumina-doped silica aerogel (50 mW m^{-1}-k at room temperature).[39]

The ultralow thermal conductivity in SiOC aerogels is primarily due to their nanostructured, highly porous framework that restricts heat flow through solid, gaseous, and radiative paths. Mesoporosity, low density, and a tortuous network of SiOC particles combine to suppress all modes of thermal transport. This remarkable characteristic is coupled with outstanding thermal stability up to 1000 °C. Such impressive thermal properties are crucial in various industrial applications.

The thermal stability of transparent SiOC aerogels treated at 800 °C was evaluated using thermal gravimetric analysis in air, as shown in Fig. 14. The TGA results show a slight weight gain of 1.9 % wt, 1.1 % wt, and 0.9 % wt for the B2T 800, BT 800 and BT2 800 samples, respectively. This weight gain is attributed to the oxidation of Si–C to Si–O bonds, probably involving Si–CH_x bonds following the reaction.[40]

$$Si - CH_x + O_2 \rightarrow Si - O + xH_2O/CO$$

The DTA curve shows a single exothermic peak at 520 °C and 530 °C for the BT800 and BT2800 samples, respectively. In

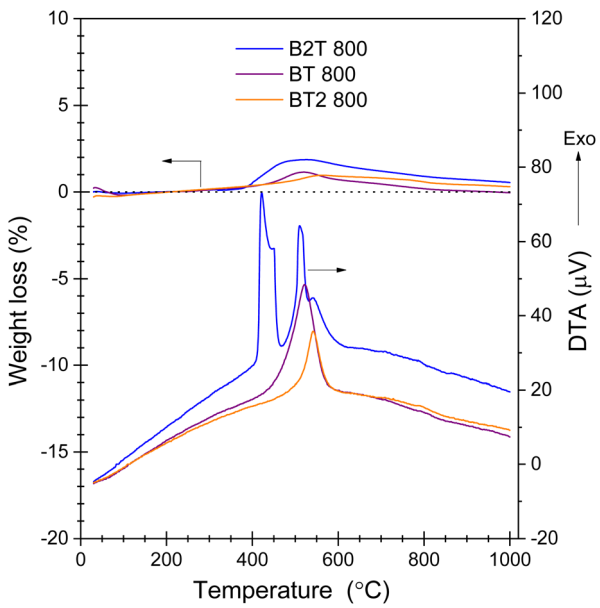

Fig. 14 DTA-TGA curves of SiOC glasses (B2T 800, BT 800 and BT2 800) treated in pure air. The black dotted line indicates zero weight loss. The gradual decline of the TGA curve above 600 °C is probably due to the buoyancy effect of the instrument. The SiOC glasses were thermally stable in an oxidative atmosphere up to 500 °C and a small weight increase (1–2 wt%) was observed from 400 to 500 °C.

contrast, the B2T800 sample exhibits two exothermic peaks: one at 420 °C and another at 510 °C. The 510 °C peak may be associated with the oxidation of Si–CH_x units, similar to those present in the BT800 and BT2800 samples. The additional peak at 420 °C observed in the B2T800 sample—which has a higher carbon content than the other two—could be attributed to Si–CH_x units that are richer in hydrogen.

Studies have demonstrated that SiOC materials show excellent oxidation resistance; however, their thermal stability in air is influenced by several parameters, such as composition (specifically free carbon content), porosity and pyrolysis temperature. Free carbon within the SiOC structure results in oxidative degradation, leading to weight loss at 300 °C, while the oxidation of the Si–C bonds results in a weight gain above 1000 °C.[40,41] Non-porous SiOC materials exhibit superior oxidation resistance by forming a thin oxide layer that acts as a oxygen barrier diffusion.[42,43] Furthermore, a higher pyrolysis temperature in PDCs leads to an increased formation of free carbon for precursors with a high carbon content, which accelerates oxidation at elevated temperatures. In this study, despite the high porosity of the SiOC samples, the stoichiometric and low-carbon composition of the hybrid aerogels enables the SiOC materials to exhibit excellent thermal stability in an oxidative atmosphere up to 1000 °C.[44]

Optical properties. Fig. 15 illustrates the optical transmittance of B2T 800, BT 800 and BT2 800 samples. All SiOC samples exhibit low optical transmittance at short wavelengths due to structural inhomogeneities. The microstructure is composed of 80 to 90% air-filled pores, ranging from 15 to 25 nm in size. The presence of these nanosized pores reduces optical transmittance in the UV-vis wavelength range due to Rayleigh scattering.[45,46] The scattering intensity is proportional to λ^{-4}, indicating that structural inhomogeneity tends to scatter short wavelengths compared to longer wavelengths.

The optical transparency of SiOC aerogels is influenced by bulk density, particle size and pore size. Notably, the transmittance of the SiOC aerogels slightly increased as the bulk density rose from 0.25 g cm^{-3} in the BT2 800 sample to ~0.40 g cm^{-3} in the BT 800 and B2T 800 samples. The SiOC aerogels, particularly BT2 800, demonstrated a combination of high transparency (>80% at $\lambda \geq 800$ nm), lowest thermal conductivity (~15 mW m^{-1}-k) and excellent stability in pure air.

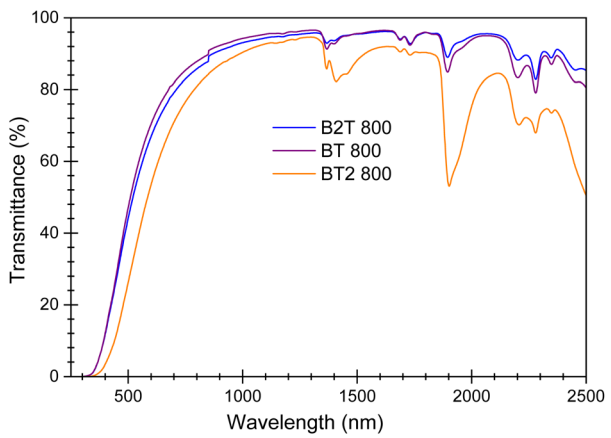

Fig. 15 Transmission spectra of 2 mm-thick SiOC aerogels in the UV–vis wavelength.

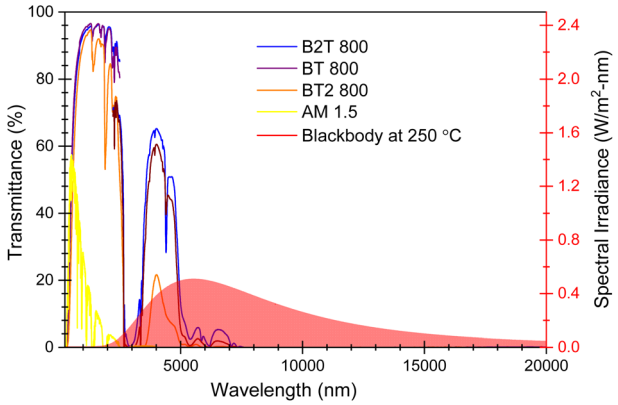

Fig. 16 Transmission spectra of 2 mm thick SiOC aerogels in the UV–Vis–IR ranges. Transmittance of transparent SiOC aerogels compared with the AM1.5 solar spectrum (yellow line) and blackbody at 250 °C (red area).

Fig. 16 presents the transmission spectra of the SiOC aerogels up to 20 000 nm. The SiOC aerogels combine high optical transparency in the visible-NIR region with strong IR absorption ($\lambda > 3$ μm), a particularly advantageous feature for solar thermal applications. The high NIR transmittance allows most of the solar spectrum to pass through the aerogel and reach the absorber, while the strong long-wavelength absorption suppresses radiative heat losses by trapping thermal radiation within the material. This dual functionality optimizes solar energy input and minimizes radiative losses, thereby improving the overall efficiency of the solar thermal systems.

Conclusions

This study synthesizes transparent SiOC aerogels utilizing low-carbon-containing silicon alkoxide precursors. The materials demonstrated high thermal stability, achieving a surface area of 855 m^2 g^{-1}, a porosity of 90%, and a pore volume of 3, 9 cm^3 g^{-1} for gels annealed at 1000 °C. The SiOC ceramics, derived from either pure bridged CH_2 precursor or a combination of CH_2 and Si–H precursors, displayed mesoporous characteristics. The structure and microstructural properties of the SiOC ceramics were primarily influenced by the amount of TREOS in the initial precursors and the pyrolysis temperature. The increased pore volume, porosity, and pore size can be attributed to TREOS; however, the relationship with surface area is more complex, as it is related to both smaller pore size and higher pore volume. Notably, as the pyrolysis temperature rose, many properties including surface area, porosity, and pore volume showed a slight decrease.

The thermal conductivity of porous SiOC ceramics ranges from 15 to 60 mW m^{-1}-K for hybrid aerogels pyrolyzed at 800 °C and from 35 to 156 mW m^{-1}-K for those treated at 1000 °C. The stoichiometric SiOC aerogel treated at 800 °C exhibits

exceptionally low thermal conductivities, reaching as low as 15 mW m^{-1}-K. This value is comparable to preceramic aerogels, yet this material retains high thermal stability up to 1000 °C. This ultralow thermal conductivity for ceramic aerogel is attributed to its low bulk density, high porosity, and mesopores. Additionally, this material also shows a unique combination of high solar transmittance and infrared absorption, further enhancing the overall performance of the insulating properties of the transparent materials. These characteristics make the synthesized SiOC ceramic aerogels well-suited for use in thermal collectors operating at high temperatures. In terms of scalability of the SiOC aerogel fabrication process, we do not anticipate major challenges beyond those already resolved in the production of large monolithic transparent silica aerogels, which are already commercially available. The key requirements are access to a large supercritical dryer and a high-capacity furnace for pyrolysis.

Author contributions

A. M. Abebe: conceptualization, methodology, formal analysis, investigation, writing – original draft, writing – review & editing, visualization, M. Biesuz: conceptualization, methodology, writing – review & editing, supervision; C. Vakifahmetoglu: review & editing, supervision; M. Cassetta: investigation, formal analysis; A. Martucci: investigation, formal analysis; G. D. Sorarù: conceptualization, methodology, resources, writing – review & editing, supervision, project administration, funding acquisition.

Conflicts of interest

There are no conflicts to declare.

Data availability

Supplementary information: The data supporting this article have been included as part of the SI. See DOI: **https://doi.org/10.1039/d5ta05778g**.

Acknowledgements

This work was financially supported by the University of Trento through the PhD program (Grant No. 000040201518). The authors also thank the Centro Piattaforme Tecnologiche at the University of Verona (Italy) for providing access to advanced scientific instrumentation and technical support.

References

1 P. Colombo, G. Mera, R. Riedel and G. D. Sorarù, *J. Am. Ceram. Soc.*, 2010, **93**, 1805–1837.
2 Q. Wen, Z. Yu and R. Riedel, *Prog. Mater. Sci.*, 2020, **109**, 100623.
3 G. Mera, A. Navrotsky, S. Sen, H. J. Kleebe and R. Riedel, *J. Mater. Chem. A*, 2013, **1**, 3826–3836.
4 C. Stabler, E. Ionescu, M. Graczyk-Zajac, I. Gonzalo-Juan and R. Riedel, *J. Am. Ceram. Soc.*, 2018, **101**, 4817–4856.
5 D. Assefa, E. Zera, R. Campostrini, G. D. Soraru and C. Vakifahmetoglu, *Ceram. Int.*, 2016, **42**, 11805–11809.
6 P. R. Aravind and G. D. Sorarù, *Microporous Mesoporous Mater.*, 2011, **142**, 511–517.
7 G. D. Sorarù, E. Zera and R. Campostrini, in *Handbook of Sol-Gel Science and Technology*, ed. L. Klein, M. Aparico and A. Jitianu, Springer International Publishing, Switzerland, 2016, pp. 1–25.
8 C. Vakifahmetoglu, T. Semerci, A. Gurlo and G. D. Soraru, *Curr. Opin. Solid State Mater. Sci.*, 2021, **25**, 100936.
9 A. K. Singh and C. G. Pantano, *J. Am. Ceram. Soc.*, 1996, **79**, 2696–2704.
10 A. Quaranta, A. Karakuscu and G. D. Sorarù, in *Polymer Derived Ceramics: from Nano-Structure to Applications*, ed. P. Colombo, R. Riedel, G. D. Sorarù and H. J. Kleebe, DEStech Publications, Lancaster, Pennsylnania, 2010, pp. 253–261.
11 G. D. Sorarù, G. D'Andrea, R. Campostrini, F. Babonneau and G. Mariotto, *J. Am. Ceram. Soc.*, 1995, **78**, 379–387.
12 G. D. Sorarù, *J. Sol-Gel Sci. Technol.*, 1994, **2**, 843–848.
13 E. Abraham, V. Cherpak, B. Senyuk, J. B. ten Hove, T. Lee, Q. Liu and I. I. Smalyukh, *Nat. Energy*, 2023, **8**, 381–396.
14 R. Baetens, B. P. Jelle and A. Gustavsen, *Energy Build.*, 2011, **43**, 761–769.
15 L. Zhao, B. Bhatia, S. Yang, E. Strobach, L. A. Weinstein, T. A. Cooper, G. Chen and E. N. Wang, *ACS Nano*, 2019, **13**, 7508–7516.
16 K. McEnaney, L. Weinstein, D. Kraemer, H. Ghasemi and G. Chen, *Nano Energy*, 2017, **40**, 180–186.
17 E. Strobach, B. Bhatia, S. Yang, L. Zhao and E. N. Wang, *APL Mater.*, 2019, **7**, 081104.
18 L. Wu, B. Zhao, D. Gao, D. Jiao, M. Hu and G. Pei, *Carbon Neutrality*, 2023, **2**, 6.
19 L. An, Z. Li, Z. Guo, Y. Hu, Y. Huang, J. N. Armstrong, C. Zhou and S. Ren, *Nanoscale Adv.*, 2022, **4**, 4291–4295.
20 Y. Sun, R. Wilson and Y. Wu, *Appl. Energy*, 2018, **226**, 713–729.
21 Z. J. Berquist, A. J. Gayle, N. P. Dasgupta and A. Lenert, *Adv. Funct. Mater.*, 2022, **32**, 1–9.
22 A. M. Abebe, M. Biesuz, C. Vakifahmetoglu, M. Cassetta and G. D. Sorarù, *J. Sol-Gel Sci. Technol.*, 2025, **114**, 1117–1126.
23 G. D. Sorarù, S. Modena, P. Bettotti, G. Das, G. Mariotto and L. Pavesi, *Appl. Phys. Lett.*, 2003, **83**, 749–751.
24 R. Campostrini, *J. Mater. Chem.*, 1996, **6**, 585–594.
25 D. Bahloul-Hourlier, J. Latournerie and P. Dempsey, *J. Eur. Ceram. Soc.*, 2005, **25**, 979–985.
26 P. Hubert Mutin, *J. Am. Ceram. Soc.*, 2002, **85**, 1185–1189.
27 C. Stabler, A. Reitz, P. Stein, B. Albert, R. Riedel and E. Ionescu, *Materials*, 2018, **11**, 1–18.
28 T. Rouxel, G. D. Soraru and J. Vicens, *J. Am. Ceram. Soc.*, 2001, **84**, 1052–1058.
29 M. Graczyk-Zajac, D. Vrankovic, P. Waleska, C. Hess, P. V. Sasikumar, S. Lauterbach, H. J. Kleebe and G. D. Sorarù, *J. Mater. Chem. A*, 2018, **6**, 93–103.

30 B. Toury and F. Babonneau, *J. Eur. Ceram. Soc.*, 2005, **25**, 265–270.
31 A. D. Chomel, P. Dempsey, J. Latournerie, D. Hourlier-Bahloul and U. A. Jayasooriya, *Chem. Mater.*, 2005, **17**, 4468–4473.
32 B. Riegel, I. Hartmann, W. Kiefer, J. Groß and J. Fricke, *J. Non-Cryst. Solids*, 1997, **211**, 294–298.
33 B. Humbert, A. Burneau, J. P. Gallas and J. C. Lavalley, *J. Non-Cryst. Solids*, 1992, **143**, 75–83.
34 G. Spiekermann, M. Steele-Macinnis, C. Schmidt and S. Jahn, *J. Chem. Phys.*, 2012, **136**, 154501.
35 F. Wang, L. Cheng and S. Liang, *Appl. Compos. Mater.*, 2019, **26**, 1411–1422.
36 L. Cheng, Y. Xu, Q. Zhang and L. Zhang, *Carbon*, 2003, **41**, 707–711.
37 O. Icin, A. M. Abebe, G. D. Soraru and C. Vakifahmetoglu, *J. Am. Ceram. Soc.*, 2024, **107**, 6729–6740.
38 H. Yang, C. Li, X. Yue, J. Huo, F. Ye, J. Liu, F. Shi and J. Ma, *Mater. Des.*, 2020, **185**, 108217.
39 Y. Wu, X. Wang, L. Liu, Z. Zhang and J. Shen, *Gels*, 2021, **7**, 122.
40 J. Parmentier, G. D. Soraru and F. Babonneau, *J. Eur. Ceram. Soc.*, 2001, **21**, 817–824.
41 M. A. Mazo, A. Nistal, A. C. Caballero, F. Rubio, J. Rubio and J. L. Oteo, *J. Eur. Ceram. Soc.*, 2013, **33**, 1195–1205.
42 R. H. Doremus and S. Prochazka, *J. Mater. Res.*, 1991, **6**, 2716–2722.
43 S. Modena, G. D. Sorarù, Y. Blum and R. Raj, *J. Am. Ceram. Soc.*, 2005, **88**, 339–345.
44 K. Lu and D. Erb, *Int. Mater. Rev.*, 2018, **63**, 139–161.
45 B. Merillas, J. Martín-De León, F. Villafañe and M. A. Rodríguez-Pérez, *ACS Appl. Polym. Mater.*, 2021, **3**, 4607–4615.
46 X. Xu, Q. Zhang, M. Hao, Y. Hu, Z. Lin, L. Peng, T. Wang, X. Ren, C. Wang, Z. Zhao, C. Wan, H. Fei, L. Wang, J. Zhu, H. Sun, W. Chen, T. Du, B. Deng, G. J. Cheng, I. Shakir, C. Dames, T. S. Fisher, X. Zhang, H. Li, Y. Huang and X. Duan, *Science*, 2019, **363**, 723–727.